Applied Radiation and Isotopes 227 (2026) 112288

Contents lists available at ScienceDirect

Applied Radiation and Isotopes

journal homepage: www.elsevier.com/locate/apradiso

Structural and luminescence properties of alkali-co-doped $LiCaBO_3$: Dy^{3+} phosphors

M.B. Coban [a], Jabir Hakami [b], H. Aydin [c,d], U.H. Kaynar [e], E. Aymila Çin [f], T. Karaman [f], M. Sharahili [b], O. Madkhali [b], D. Somaily [b], Rachid Karmouch [b], N. Can [b,*]

[a] Balikesir University, Faculty of Arts and Sciences, Department of Physics, Balikesir, Turkiye
[b] Jazan University, College of Science, Department of Physical Sciences, Physics Division, P.O. Box 114, 45142, Jazan, Saudi Arabia
[c] Graphene Application&Research Center, Izmir Katip Celebi University, Izmir, Turkiye
[d] Central Research Laboratories, Izmir Katip Celebi University, Izmir, Turkiye
[e] Bakırcay University, Faculty of Engineering and Architecture, Department of Fundamental Sciences, Menemen, Izmir, Turkiye
[f] Bakırcay University, Graduate School of Natural and Applied Sciences, Menemen, Izmir, Turkiye

ARTICLE INFO

Keywords:
$LiCaBO_3$ phosphors
Photoluminescence
Judd–Ofelt analysis
Concentration quenching
White light emission
Thermal stability

ABSTRACT

Dysprosium (Dy^{3+})-doped lithium calcium borate ($LiCaBO_3$, LiCOB) phosphors were synthesized via a sol–gel combustion route and systematically investigated with respect to their structural, vibrational, and luminescence characteristics, with emphasis on the role of alkali co-doping (Na^+, K^+). XRD with Rietveld refinement confirmed the orthorhombic phase formation, indicating that Dy^{3+} ions substitute Ca^{2+} sites, while alkali co-doping provided effective charge compensation and mitigated lattice strain. FTIR and Raman analyses verified the preservation of the borate framework, with Na^+ yielding more efficient structural stabilization than K^+. Photoluminescence spectra revealed the characteristic Dy^{3+} blue ($^4F_{9/2} \rightarrow {}^6H_{15/2}$) and yellow ($^4F_{9/2} \rightarrow {}^6H_{13/2}$) emissions, enabling quasi-white light generation. The emission intensity was maximized at 2 wt% Dy^{3+}, with quenching beyond this level governed by dipole–quadrupole interactions, as confirmed by Dexter analysis. Alkali co-doping significantly enhanced PL output, with Na^+ producing stronger and more stable emission than K^+ due to superior charge compensation. Judd–Ofelt analysis based on emission spectra yielded Ω_2, Ω_4, and Ω_6 parameters consistent with experimental lifetimes, demonstrating that Na^+ co-doping promotes red-shifted transitions via enhanced Ω_6, whereas K^+ favors yellow emission through Ω_2 enhancement. Remarkably, temperature-dependent PL studies showed anomalous thermal enhancement in Dy^{3+}-only samples, while Na^+/K^+ co-doped systems exhibited trap-assisted recovery with low activation energies (0.21–0.22 eV), indicating excellent thermal stability. Chromaticity coordinates confirmed tunable near-white emission, underlining the potential of alkali-modified LiCOB:Dy^{3+} phosphors not only for solid-state lighting but also for future radiation detector applications.

1. Introduction

Borate-based compounds have attracted considerable attention in solid-state physics and materials science owing to their wide band gap, low phonon energy, high thermal stability, and structural versatility (Padlyak and Drzewiecki, 2013). Compared with silicates and phosphates, borates exhibit lower phonon energies and enhanced charge-transfer efficiency, while offering higher thermal and chemical stability than halide hosts, making them particularly suitable for optoelectronic applications (Adeleye et al., 2024; Blasse and Grabmaier, 1994; Yen et al., 2007). As a result, borates are considered excellent host materials for rare-earth (RE) activators, enabling efficient luminescence in the ultraviolet–visible spectral range and supporting applications in photonics, nonlinear optics, and radiation dosimetry (Oza et al., 2015). Among the various borate hosts, lithium calcium borate ($LiCaBO_3$, hereafter LiCOB) has emerged as a promising candidate because of its relatively low effective atomic number ($Z_{eff} \approx 14.9$), high radiation sensitivity, and capability to crystallize in an orthorhombic structure with excellent phase stability (Beck et al., 2017; Li et al., 2010; Sharma et al., 2024). Moreover, LiCOB has been explored as a nonlinear optical crystal with notable birefringence, expanding its application potential beyond conventional phosphor technologies (Chen et al., 1989).

* Corresponding author.
E-mail address: ncan@jazanu.edu.sa (N. Can).

https://doi.org/10.1016/j.apradiso.2025.112288
Received 3 October 2025; Received in revised form 23 October 2025; Accepted 24 October 2025
Available online 1 November 2025

Beyond the specific host lattice, Dy^{3+} ions are known to play a versatile role in luminescent processes due to their unique $4f^9$ electronic configuration, which supports both magnetic dipole and hypersensitive electric dipole transitions. These transitions yield characteristic blue ($^4F_{9/2} \rightarrow {}^6H_{15/2}$) and yellow ($^4F_{9/2} \rightarrow {}^6H_{13/2}$) emissions that are efficiently excited under cathodoluminescence (CL), photoluminescence (PL), or thermoluminescence (TL) conditions. In cathodoluminescence studies, Dy^{3+} centers have been shown to act as effective recombination sites, contributing to intense blue–yellow emissions irrespective of the host matrix (Ayvacikli et al., 2020a; Roman-Lopez et al., 2012). Similarly, in TL-based materials such as $CaSO_4$:Dy, Dy^{3+} ions serve as electron–hole recombination centers that govern trap-controlled glow peaks and high dosimetric sensitivity (Roman-Lopez et al., 2012; Boronat et al., 2023). This dual functionality—acting as a luminescent activator and a recombination center—renders Dy^{3+} a particularly attractive dopant for both optical and radiation-induced luminescence systems. Such versatility underscores the importance of understanding Dy^{3+}-related energy transfer mechanisms independently of the host matrix, as pursued in the present work.

Rare-earth doping in borate matrices has been widely explored, with activators such as Eu^{3+}, Tb^{3+}, Sm^{3+}, and Ce^{3+} studied for their distinctive emission characteristics (Li et al., 2010; Padlyak and Drzewiecki, 2013). In this context, dysprosium (Dy^{3+}) holds particular interest because it exhibits two strong and complementary emission bands: a blue emission around 480 nm corresponding to the $^4F_{9/2} \rightarrow {}^6H_{15/2}$ magnetic dipole transition and a yellow emission near 575 nm due to the $^4F_{9/2} \rightarrow {}^6H_{13/2}$ hypersensitive electric dipole transition (Altowyan et al., 2025b; Luewarasirikul et al., 2026; Nasreen et al., 2025). The relative intensity balance between these two emissions enables quasi-white light generation, positioning Dy^{3+}-activated phosphors as potential candidates for white light-emitting diodes (WLEDs) and solid-state lighting (Bajaj and Omanwar, 2012). Furthermore, Dy^{3+} ions can act as efficient luminescence centers in thermoluminescence (TL) processes, where defect-mediated trapping and recombination contribute to radiation dosimetry applications (Aljewaw et al., 2023; Jiang et al., 2008; Khan et al., 2016; Oza et al., 2015).

Previous investigations have demonstrated that Dy^{3+}-doped borate systems, including $Li_2B_4O_7$, CaB_4O_7, and $LiCaBO_3$, display efficient PL and TL properties (Bajaj and Omanwar, 2012; Padlyak and Drzewiecki, 2013). For example, Bajaj & Omanwar (Bajaj and Omanwar, 2012) reported well-resolved TL glow peaks in LiCOB:Dy^{3+}, with linear dose response under X-ray irradiation, while Oza et al. (2015) showed that Dy^{3+}-doped LiCOB exhibited high TL sensitivity, stability against fading, and reproducibility under γ-ray and heavy ion beam exposure. More recently, Sharma et al. (2024) emphasized the thermal stability and chromaticity optimization of LiCOB:Dy^{3+}, highlighting its dual potential in optoelectronic and dosimetric domains. Despite these advancements, key aspects such as the Dy^{3+} local environment, concentration quenching behavior, and detailed radiative properties in the LiCOB matrix remain insufficiently understood, necessitating further systematic investigation. In particular, the combined effect of alkali co-doping and Dy^{3+} incorporation on luminescence performance has not been systematically explored. To the best of our knowledge, no prior study has simultaneously investigated alkali co-doping strategies and performed emission-based Judd–Ofelt analysis in Dy^{3+}-activated LiCOB phosphors. This represents a critical gap in the literature, which the present study seeks to address through a comprehensive structural and optical characterization approach.

In the present work, Dy^{3+}-activated LiCOB phosphors were comprehensively investigated in terms of their structural, vibrational, morphological, and optical characteristics using XRD with Rietveld refinement, Raman and FTIR spectroscopy, SEM/EDS, and photoluminescence (PL) studies, including lifetime and CIE chromaticity analyses. Particular emphasis was placed on Judd–Ofelt (J–O) analysis for evaluating the radiative properties of Dy^{3+}. While conventional J–O analysis relies on absorption spectra, such measurements are often impractical for polycrystalline or nanocrystalline powders. To overcome this limitation, alternative approaches reported in the literature—such as excitation spectrum substitution (Luo et al., 2010), emission-based J–O analysis (Ćirić et al., 2019; Zhang et al., 2024), diffuse-reflectance methods (Xue et al., 2020), and fluorescence decay-based models (Luo et al., 2020)—were considered. In addition, the LiCOB host lattice was co-doped with monovalent alkali ions (K^+ and Li^+), which are known to modify the local crystal field environment and participate in charge compensation mechanisms. Such effects influence defect structure and energy transfer dynamics, thereby enhancing the luminescence efficiency of Dy^{3+} activators. While earlier reports on Eu^{3+}, Sm^{3+}, Tb^{3+}, and Ce^{3+} doping in LiCOB partially considered alkali co-doping for charge compensation (Li et al., 2010; LI et al., 2009), most investigations centered on Dy^{3+}—including recent ones (Beck et al., 2017; Oza et al., 2015; Sharma et al., 2024)—have not explicitly addressed this aspect. Thus, the influence of alkali co-doping on charge compensation and Dy^{3+} luminescence efficiency remains ambiguous, constituting a key research gap that this work seeks to address. Accordingly, the present study aims to systematically investigate Dy^{3+}-doped LiCOB with controlled alkali co-doping in order to achieve charge balance and optimize luminescence performance. Following these advancements, J–O analysis was implemented here based on the measured PL spectra, enabling the calculation of radiative transition probabilities, branching ratios, and emission cross-sections. This integrated methodology not only deepens the understanding of Dy^{3+} optical behavior in LiCOB but also reinforces its applicability as a dual-functional material for white light emission and radiation dosimetry.

2. Experiments

2.1. Synthesis of Dy^{3+}-doped and (Na^+/K^+) co-doped $LiCaBO_3$

$LiCaBO_3$ phosphors were synthesized via a sol–gel combustion route using urea as fuel. High-purity precursors were used without further purification: lithium nitrate ($LiNO_3$, Sigma, ≥99.99 %), calcium nitrate ($Ca(NO_3)_2{\cdot}xH_2O$, Sigma-Aldrich, ≥99.9 %), boric acid (H_3BO_3, Merck), and urea ($CO(NH_2)_2$). Dysprosium nitrate ($Dy(NO_3)_3{\cdot}xH_2O$) was used as the activator (dopant), while sodium nitrate ($NaNO_3$, Merck, 99.9 %) and potassium nitrate (KNO_3, Merck, 99.9 %) served as co-dopant sources. Dy^{3+} was introduced at concentrations of 0.5, 1, 2, 3, 5 and 7 wt%, and co-doping with Na^+ or K^+ was carried out at mass percentages of 0.5, 1, 2, 3, 5 and 7 wt%. In a typical preparation, stoichiometric amounts of $LiNO_3$ and $Ca(NO_3)_2$ were dissolved in 20 mL of distilled water in a quartz beaker, followed by the addition of H_3BO_3 and urea. When required, $Dy(NO_3)_3$ together with $NaNO_3$ or KNO_3 was also added. The solution was magnetically stirred at 80 °C for 1 h with the beaker covered to ensure complete dissolution and homogenization. Afterwards, the cover was removed and stirring continued at the same temperature until excess water was evaporated and the solution gradually transformed into a viscous gel. The resulting gel was then subjected to microwave-assisted ignition in a domestic microwave oven. Within a short time, vigorous combustion accompanied by dense fume evolution occurred, yielding a porous, fluffy white powder.

The as-combusted powders were collected and calcined in air at 800 °C for 2 h to remove residual organics and improve crystallinity. The calcination was carried out with a controlled heating rate of 5 °C min^{-1}, followed by natural cooling to room temperature at an approximate rate of 3 °C min^{-1}. The overall combustion reaction can be expressed as:

$$2\,LiNO_3 + 2\,Ca(NO_3)_2 + 2\,H_3BO_3 + 5\,CO(NH_2)_2 \rightarrow 2\,LiCaBO_3 + \text{gaseous products } (NO_x,\ CO_2,\ H_2O,\ NH_3,\ \ldots)$$

After calcination, the white nano-sized $LiCaBO_3$ powders were cooled to room temperature and stored in a desiccator until further characterization.

2.2. Characterization techniques

The prepared $LiCaBO_3$:Dy^{3+} and alkali co-doped phosphor samples were thoroughly characterized using a range of complementary analytical techniques to establish their structural integrity, vibrational features, surface morphology, and luminescence performance.

X-ray diffraction (XRD) measurements were performed on a Malvern PANalytical Empyrean diffractometer employing Cu Kα radiation (λ = 1.5406 Å) operated at 40 kV and 40 mA. Diffraction data were collected in the 2θ range of 10°–80° with a step size of 0.02° and a scan rate of 1° min^{-1}. Structural refinement and phase identification were carried out using the Rietveld method implemented in *HighScore Plus* software. Fourier-transform infrared (FTIR) spectra were acquired on a *Thermo Scientific Nicolet iS50* spectrometer in the 4000–400 cm^{-1} range using KBr pellets prepared with finely ground samples. Each spectrum was averaged over 32 scans at a spectral resolution of 4 cm^{-1} to ensure accurate identification of the borate vibrational modes. Raman spectroscopy was conducted on a *Renishaw inVia Reflex* spectrometer equipped with a 532 nm excitation laser and a 2400 lines mm^{-1} grating. The laser power was kept below 1 mW to avoid local heating, and each spectrum was collected in the 200–1600 cm^{-1} range with an accumulation time of 10 s per scan. Surface morphology and chemical composition were analyzed using a *ZEISS GeminiSEM 500* scanning electron microscope (SEM) operated at 10 kV accelerating voltage, coupled with energy-dispersive X-ray spectroscopy (EDS) for elemental mapping. All samples were sputter-coated with a thin (~10 nm) gold layer to minimize surface charging during imaging. Photoluminescence (PL) excitation and emission spectra were recorded on an *Edinburgh Instruments FS5 spectrofluorometer* equipped with a 150 W xenon arc lamp as the excitation source. The slit width was maintained at 2.5 nm for both excitation and emission channels. Fluorescence decay profiles were measured using a pulsed xenon lamp with a 5 μs dwell time, and the average lifetimes were obtained from multi-exponential fitting. To assess thermal stability, temperature-dependent PL spectra were collected in the 300–550 K range using a *Linkam THMS600* variable-temperature stage. The samples were heated at a rate of 5 °C min^{-1} to the desired temperature, held for 5 min for thermal equilibrium, and then allowed to cool naturally to room temperature at approximately 3 °C min^{-1}. This procedure ensured reproducible evaluation of thermal quenching and trap-assisted luminescence behavior.

3. Results and discussions

3.1. Structural analysis (XRD and rietveld refinement)

The XRD patterns of undoped and Dy^{3+}-doped $LiCaBO_3$ (LiCBO) samples, with and without alkali co-doping, are shown in Fig. 1a. All diffraction peaks are in good agreement with the standard JCPDS card No. 98-009-9386, confirming the orthorhombic crystal structure (Sharma et al., 2024). No secondary phases or impurity peaks were detected, indicating successful incorporation of Dy^{3+} ions and the chemical stability of the host lattice. The major diffraction peaks, such as (002), (200), (211), and (132), remain unchanged after Dy^{3+} or alkali co-doping, suggesting that the overall crystal structure is preserved.

The Rietveld refinement profiles (Fig. 1b) further validate the phase purity and crystallographic consistency of the samples. The refinement parameters, including χ^2, R_p, R_{wp}, and R_{exp} (Table 1), are within acceptable limits, confirming the reliability of the fitting. The refined lattice parameters show slight variations upon Dy^{3+} doping and alkali co-doping. For example, the unit cell volume increased from 497.99 $Å^3$ (undoped) to 499.29 $Å^3$ for LiCBO:0.02Dy^{3+}, consistent with the substitution of Ca^{2+} (ionic radius 1.00 Å, CN = 6) by Dy^{3+} (0.97 Å, CN = 6).

These minor shifts suggest that $Dy^{3+} \rightarrow Ca^{2+}$ substitution introduces a +1 local charge excess and lattice strain. Intentional alkali co-doping (Na^+ or K^+) compensates for this imbalance—most plausibly by occupying Li^+ sites—thereby restoring electroneutrality and relaxing the lattice. Consistent with this, the unit-cell volume partially returns toward the pristine value upon charge compensation, reaching 498.58 $Å^3$ for Dy^{3+}, K^+ and 498.67 $Å^3$ for Dy^{3+}, Na^+, while the refinement residuals ($\chi^2 \approx 4.18$–4.22; $R_{wp} \approx 0.158$) remain low and comparable. The Rietveld fits thus corroborate that Na^+/K^+ co-doping mitigates Dy^{3+}-induced strain without generating secondary phases.

The crystal structure model of Dy^{3+}-doped LiCBO, shown in Fig. 1c, illustrates that Dy^{3+} ions preferentially substitute Ca^{2+} sites rather than Li^+ sites. This substitution is supported by the calculated ionic radius mismatch (D_r) values presented in Table 2. The mismatch between Ca^{2+} and Dy^{3+} is 8.8 % for CN = 6 and 8.49 % for CN = 7, both well below the 30 % limit for stable substitution. In contrast, the mismatch between Li^+ and Dy^{3+} is much larger—62.13 % for CN = 5 and 20 % for CN = 6—clearly ruling out Dy^{3+} substitution at the Li^+ site. The results indicate that Dy^{3+} ions occupy Ca^{2+} sites in the LiCBO lattice.

These minor shifts suggest that $Dy^{3+} \rightarrow Ca^{2+}$ substitution introduces a +1 local charge excess and lattice strain. Intentional alkali co-doping (Na^+ or K^+) compensates for this imbalance—most plausibly by occupying Li^+ sites—thereby restoring electroneutrality and relaxing the lattice. Consistent with this, the unit-cell volume increases from 497.99 $Å^3$ (undoped) to 499.29 $Å^3$ for LiCBO:0.02Dy^{3+}, but partially returns toward the pristine value upon charge compensation (498.58 $Å^3$ for Dy^{3+}, K^+ and 498.67 $Å^3$ for Dy^{3+},Na^+), while the refinement residuals ($\chi^2 \approx 4.18$–4.22; $R_{wp} \approx 0.158$) remain low and comparable. The Rietveld fits in Fig. 1b, thus corroborating that Na^+/K^+ co-doping mitigates Dy^{3+}-induced strain without generating secondary phases (Fig. 1c).

3.2. Vibrational analysis (FTIR and Raman spectroscopy)

The FTIR spectra of undoped and Dy^{3+}-doped LiCBO samples, with and without alkali co-doping, are shown in Fig. 2a. All samples display characteristic vibrational modes of borate groups. The broad absorption bands in the range of 1432–1200 cm^{-1} correspond to the stretching vibrations of trigonal BO_3 units, while the band near 922 cm^{-1} is attributed to the stretching of tetrahedral [BO_4] groups (Kumar et al., 2025; Mastanappa et al., 2024). Additional features at 859, 758, and 654 cm^{-1} arise from B_3–O and B–O–B linkages, and the band at 508 cm^{-1} corresponds to bending vibrations of B–O–B (Altowyan et al., 2025b). Importantly, Dy^{3+} substitution and alkali co-doping do not introduce new bands or shift the main vibrational peaks significantly, indicating that the fundamental borate framework remains intact. This stability suggests that Dy^{3+} incorporation occurs without altering the basic structural units of the LiCBO host.

Complementary insights are obtained from Raman spectroscopy (Fig. 2b). The undoped sample exhibits distinct bands associated with symmetric and asymmetric stretching modes of BO_3 and [BO_4] units, together with bending vibrations of B–O–B linkages (Kumar et al., 2025; Li et al., 2010). Upon Dy^{3+} doping, the spectra show a slight broadening and intensity variation of certain bands, reflecting local distortions within the borate network. In contrast, the spectra of co-doped (Na^+, K^+) samples reveal different behaviors: Na^+ co-doping tends to preserve sharper features, indicating effective charge compensation, whereas K^+ co-doping induces comparatively broader bands, consistent with increased lattice disorder. These findings confirm that alkali ions primarily act as charge compensators, with Na^+ providing more efficient stabilization of the borate framework than K^+. This interpretation is in line with the XRD and Rietveld results, where the orthorhombic crystal structure was preserved.

3.3. Photoluminescence excitation and emission spectra

The photoluminescence excitation (PLE) and emission (PL) spectra of LiCBO:0.005Dy^{3+} phosphors are shown in Fig. 3. The PLE spectrum, monitored at the strongest emission line (λ_{em} = 609 nm, corresponding to the $^4F_{9/2} \rightarrow {}^6H_{13/2}$ transition), displays several sharp f–f transitions in the ultraviolet (UV) and near-UV regions. Prominent excitation peaks

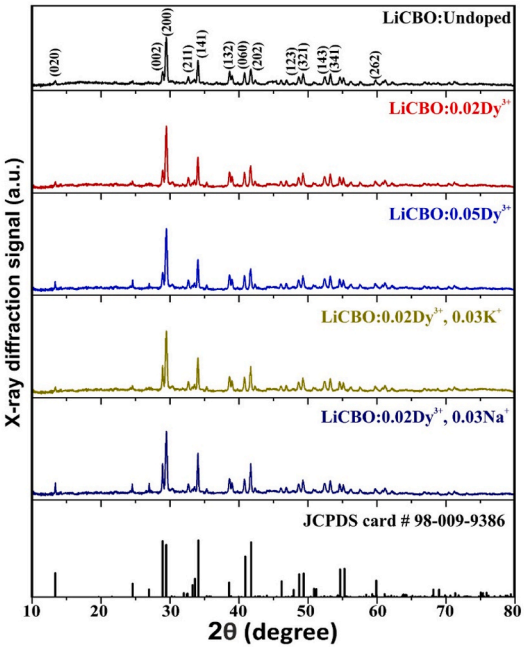

(a)

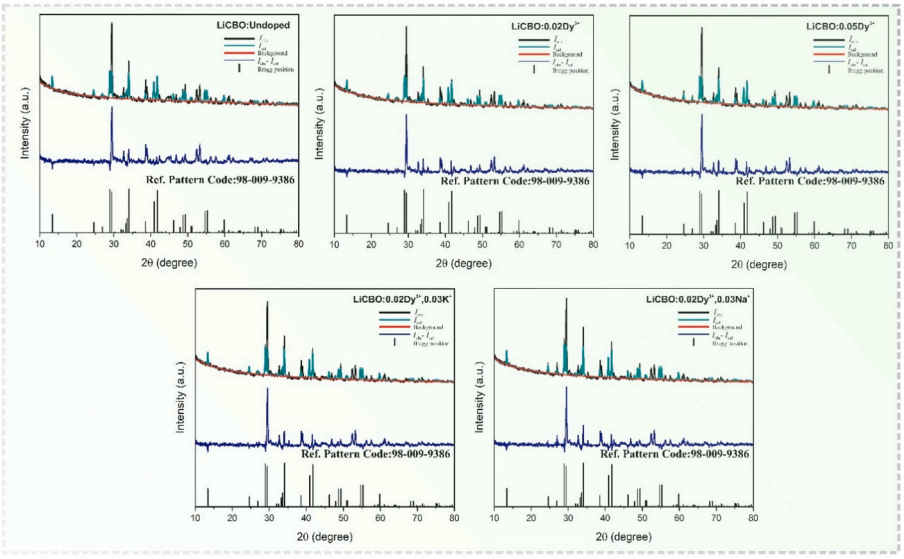

(b)

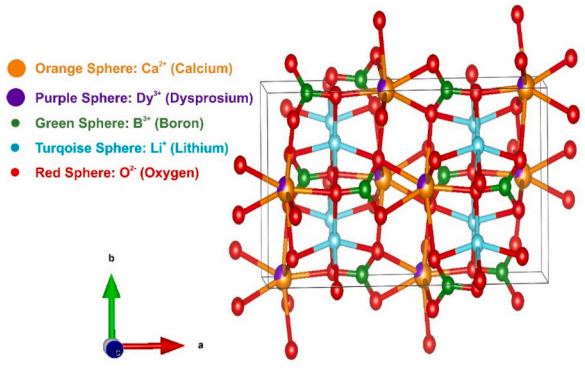

(c)

Fig. 1. (a) XRD patterns of undoped, Dy^{3+}-doped, and alkali co-doped LiCBO samples indexed to JCPDS card no. 98-009-9386, confirming orthorhombic phase formation without secondary phases. (b) Rietveld refinement profiles showing good agreement between observed and calculated patterns with low residuals. (c) Crystal structure model of LiCBO: Ca (orange), Dy (purple), B (green), Li (turquoise), and O (red); lattice axes a, b, c indicated.

Table 1
Refined lattice parameters and Rietveld fitting reliability factors for undoped and Dy^{3+} alkali co-doped $LiCaBO_3$ samples.

Unit Cell	LiCBO				
	Undoped	$0.02Dy^{3+}$	$0.05Dy^{3+}$	$0.02Dy^{3+}$,$0.03K^{+}$	$0.02Dy^{3+}$,$0.03Na^{+}$
a [Å]	6.07753	6.08333	6.08139	6.08053	6.08094
b [Å]	13.27052	13.28081	13.27544	13.2742	13.27459
c [Å]	6.17466	6.18002	6.17824	6.17712	6.17762
α,β,γ [°]	90, 90, 90	90, 90, 90	90, 90, 90	90, 90, 90	90, 90, 90
Vol. [$Å^3$]	497.9986	499.2931	498.7885	498.5812	498.6697
χ^2	4.1371	4.1796	4.1756	4.1847	4.2169
R_p	0.1092	0.1051	0.1048	0.1057	0.1072
R_{wp}	0.1569	0.1582	0.1580	0.1581	0.1590
R_{exp}	0.0379	0.0378	0.0378	0.0378	0.0377

Table 2
Ionic radius mismatch (Dr) between host cations (Ca^{2+}, Li^{+}) and Dy^{3+} for different coordination numbers (CN), demonstrating the preferential substitution of Ca^{2+} sites by Dy^{3+}.

	Ca		Dy			Li		Dy	
D_r	**R_m**	**CN**	**R_m**	**CN**	**D_r**	**R_m**	**CN**	**R_m**	**CN**
8.8	1.00	6	0.970	6	62.13	0.675	5	0.912	6
D_r	**R_m**	**CN**	**R_m**	**CN**	**D_r**	**R_m**	**CN**	**R_m**	**CN**
8.49	1.06	7	0.912	7	20	0.76	6	0.912	6

were observed at 294 nm ($^6H_{15/2} \rightarrow {}^4D_{7/2}$), 324 nm ($^6H_{15/2} \rightarrow {}^6P_{3/2}$), 350 nm ($^6H_{15/2} \rightarrow {}^6P_{7/2}$), 364 nm ($^6H_{15/2} \rightarrow {}^6P_{5/2}/{}^4I_{11/2}$), and 385 nm ($^6H_{15/2} \rightarrow {}^4M_{19/2}/{}^4K_{17/2}$) (Wang et al., 2016). In addition, a broad excitation band centered at 216 nm is observed, which can be ascribed to the $O^{2-} \rightarrow Dy^{3+}$ charge-transfer band (CTB). Similar CTB features have been reported for Dy^{3+}-doped oxide-based hosts, including borate lattices (Liang et al., 2016). These results indicate that the Dy^{3+} activators in the LiCBO lattice can be efficiently excited using both CTB transitions and intra-4f transitions, with the 385 nm excitation being particularly significant for near-UV pumped solid-state lighting applications. The corresponding emission spectrum, recorded under λ_{ex} = 385 nm excitation, exhibits characteristic Dy^{3+} transitions arising from the $^4F_{9/2}$ excited level. The most intense emission band at 576 nm is assigned to the hypersensitive electric dipole transition $^4F_{9/2} \rightarrow {}^6H_{13/2}$, while a prominent blue emission at 461 nm corresponds to the magnetic dipole transition $^4F_{9/2} \rightarrow {}^6H_{15/2}$ (Altowyan et al., 2025a). Additional emission bands were observed at 670 nm ($^4F_{9/2} \rightarrow {}^6H_{11/2}$), which appears with moderate intensity compared to the dominant blue and yellow emissions, and at 758 nm ($^4F_{9/2} \rightarrow {}^6F_{11/2}/{}^6H_{9/2}$), which is relatively weak. The coexistence of intense blue (461 nm) and yellow (576 nm) emissions provides a balanced spectral output that can be tuned toward near-white light, a well-known advantage of Dy^{3+}-activated phosphors (Bajaj and Omanwar, 2012; Beck et al., 2017). The dominance of the $^4F_{9/2} \rightarrow {}^6H_{13/2}$ transition (yellow) over the $^4F_{9/2} \rightarrow {}^6H_{15/2}$ transition (blue) reflects the hypersensitive nature of the electric dipole process, which strongly depends on the local asymmetry around Dy^{3+} ions. This suggests that Dy^{3+} occupies sites with lower inversion symmetry in the LiCBO lattice, in agreement with previous reports on Dy^{3+}-doped borate hosts (Oza et al., 2015; Sharma et al., 2024). Additional emission bands were observed at 670 nm ($^4F_{9/2} \rightarrow {}^6H_{11/2}$) and a weak deep-red band at 758 nm ($^4F_{9/2} \rightarrow {}^6H_{11/2}/{}^6H_{9/2}$), which appeared less intense compared to the dominant blue and yellow transitions. Overall, the excitation–emission analysis demonstrates that LiCBO:Dy^{3+} is effectively excitable by near-UV sources ($\lambda_{ex} \approx$ 385 nm), making it suitable for integration into white light-emitting diode (WLED) architectures. These results are summarized in Fig. 4. Furthermore, the strong hypersensitive yellow emission highlights the sensitivity of Dy^{3+} luminescence to local structural distortions, consistent with the structural modifications observed in the XRD analysis.

Furthermore, it should be noted that borate-based phosphors are partially hygroscopic, which allows the adsorption of small amounts of water on their surfaces. Under near-UV excitation (~385 nm), radiolysis of these adsorbed water molecules may occur, producing hydroxyl (OH^-) radicals weakly bonded to surface metal cations. These surface metal–hydroxyl complexes can contribute additional emission pathways through defect-assisted recombination, particularly in the blue–green spectral region. A similar radiolytic effect has been observed in insulating oxides and aluminosilicates, where surface metal–hydroxyl bonds generate visible luminescence following the reaction *e- + 2(M–OH) → H_2O + O + photons* (Garcia-Guinea et al., 2017). Although this effect has not yet been reported for $LiCaBO_3$ systems, it may partly account for minor spectral features observed in the PL emission profiles.

In Dy^{3+}-doped systems, the yellow ($^4F_{9/2} \rightarrow {}^6H_{13/2}$) emission is typically stronger than the red ($^4F_{9/2} \rightarrow {}^6H_{11/2}$) transition due to parity selection rules. However, some borate hosts, such as CaB_4O_7 and $La_2CaB_{10}O_{19}$, have been reported to display unusually intense red emission when Dy^{3+} occupies highly asymmetric, non-centrosymmetric sites (Altowyan et al., 2025b; Ayvacikli et al., 2020b). This behavior is attributed to crystal field stabilization of the $^6H_{11/2}$ level and the enhancement of electric dipole transitions. In our LiCBO:Dy^{3+} samples, the red band at 670 nm appears nearly comparable in intensity to the yellow transition at 576 nm, representing an anomalous red emission behavior compared with conventional Dy^{3+}-doped oxides. This suggests a significant degree of local asymmetry around Dy^{3+} ions, consistent with the XRD and Rietveld results, which point to lattice strain and charge imbalance effects introduced by Dy^{3+} substitution and partially compensated by alkali co-doping.

3.4. Concentration-dependent photoluminescence behavior

The PL spectra of LiCBO:xDy^{3+} (x = 0.005–0.07) samples under different excitation wavelengths (324, 350, 364, and 385 nm) are presented in Fig. 5a–d. Compared with the excitation–emission spectra shown in Fig. 4, these results reveal the influence of Dy^{3+} concentration on the luminescence intensity and quenching behavior. All spectra exhibit the characteristic Dy^{3+} emission bands centered at 461 nm ($^4F_{9/2} \rightarrow {}^6H_{15/2}$, magnetic dipole), 576 nm ($^4F_{9/2} \rightarrow {}^6H_{13/2}$, electric dipole), and weaker transitions in the red region. The relative intensities of these bands are strongly influenced by the Dy^{3+} concentration. At low doping levels (x ≤ 0.02), the emission intensity increases with Dy^{3+} concentration, reflecting efficient energy transfer from the host lattice to the activator ions. The maximum emission is observed at x = 0.02, irrespective of the excitation wavelength, indicating an optimal activator concentration. Beyond this level (x ≥ 0.03), the luminescence intensity

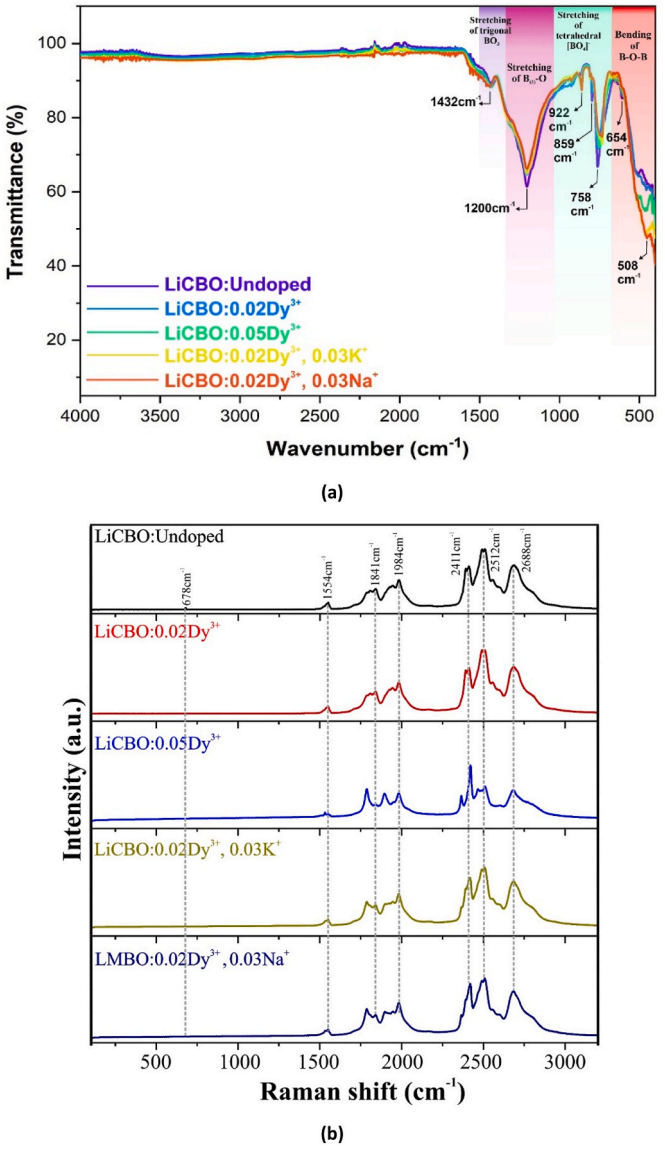

Fig. 2. (a) FTIR spectra of undoped, Dy^{3+}-doped, and alkali co-doped LiCBO samples showing characteristic vibrations of BO_3 and $[BO_4]$ units. (b) Raman spectra highlighting the effect of Dy^{3+} substitution and Na^+/K^+ co-doping on the borate network.

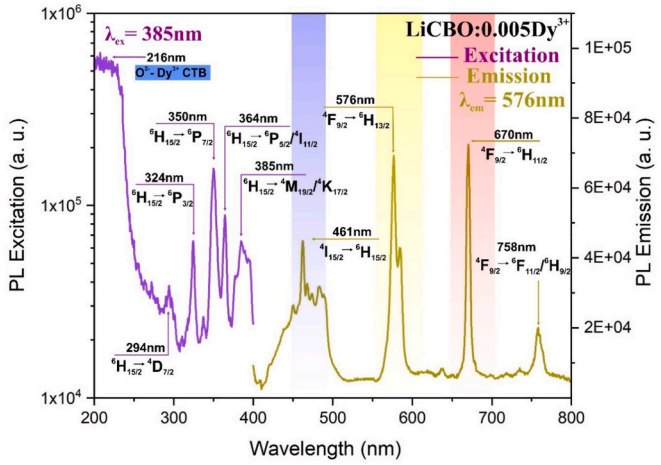

Fig. 3. (a) Excitation (λ_{em} = 609 nm) and emission (λ_{ex} = 385 nm) spectra of LiCOB:0.005Dy^{3+} phosphor at room temperature, showing the characteristic Dy^{3+} blue (461 nm) and yellow (576 nm) emissions.

decreases progressively due to concentration quenching. This quenching is attributed to enhanced non-radiative energy transfer processes between neighboring Dy^{3+} ions, as commonly observed in rare-earth-doped borates (Altowyan et al., 2025c).

At higher Dy^{3+} concentrations ($x \geq 0.03$), the PL intensity decreases due to concentration quenching, a common phenomenon in rare-earth-doped borates. Several mechanisms may account for this behavior. First, defect states generated during solid-state synthesis can act as non-radiative centers, capturing excitation energy and lowering luminescence output. Second, Dy^{3+} ions in close proximity may form quenching pairs, where energy transfer occurs between neighboring ions instead of radiative emission. Third, resonant energy transfer among Dy^{3+} ions can further reduce emission by redistributing excitation to adjacent ions that relax non-radiatively. Finally, cross-relaxation processes between Dy^{3+} ions can strongly contribute, enabling multipolar interactions that dissipate energy through non-radiative channels.

To distinguish the dominant mechanism, the critical distance (R_c) between neighboring Dy^{3+} ions was estimated using Blasse's relation (Blasse and Grabmaier, 1994):

$$R_c \approx 2\left(\frac{3V}{4\pi x_c Z}\right)^{1/3} \quad (1)$$

where V is the unit cell volume, Z is the number of cations per unit cell, and x_c is the critical Dy^{3+} concentration. To clarify the quenching mechanism, the critical transfer distance (R_c) was estimated using Blasse's relation, where V is the unit cell volume, Z is the number of cations per unit cell, and Xc is the critical Dy^{3+} concentration. When R_c exceeds 5 Å, multipolar interactions (rather than exchange interactions) dominate the energy transfer mechanism. With V = 497.99 $Å^3$, Z = 8, and x_c = 0.02, the calculated value is $R_c \approx 18.1$ Å. This provides strong evidence that the luminescence decrease in LiCBO:Dy^{3+} beyond x = 0.02 is governed mainly by multipole–multipole interactions, consistent with other Dy^{3+}-doped oxide hosts.

To further verify the concentration quenching mechanism, the experimental data were analyzed using Dexter's theory of multipolar interactions (Dexter, 1953), expressed as:

$$log(I/x) = A - (\theta/3)log(x) \quad (2)$$

where I is the emission intensity, x is the Dy^{3+} concentration, and θ indicates the type of multipolar interaction (θ = 6 for dipole–dipole, θ = 8 for dipole–quadrupole, and θ = 10 for quadrupole–quadrupole). The linear fitting of log(I/x) versus log(x) for LiCBO:xDy^{3+} (Fig. 5) yields a slope of −2.92, corresponding to θ ≈ 8.76. This value is close to the theoretical θ = 8, indicating that dipole–quadrupole interactions dominate the concentration quenching process in this system. These findings, together with the calculated critical distance ($R_c \sim 18.1$ Å), confirm that multipolar interactions between Dy^{3+} ions are the primary cause of non-radiative energy transfer at higher dopant concentrations ($x \geq 0.03$).

The excitation wavelength also plays a role in the emission profiles. Near-UV excitation at 385 nm yields the most intense PL emission, consistent with the strong absorption of Dy^{3+} in this region (Fig. 4). Excitation at 324 and 350 nm also produces strong luminescence, whereas 364 nm excitation results in slightly reduced intensity, suggesting different efficiencies of the Dy^{3+} intra-4f transitions. Importantly, the overall spectral shape remains unchanged with concentration, confirming that Dy^{3+} ions consistently substitute Ca^{2+} lattice sites without altering their local symmetry.

These results demonstrate that LiCBO:Dy^{3+} exhibits an optimal luminescence performance at x = 0.02 under near-UV excitation (λ_{ex} = 385 nm), beyond which concentration quenching dominates. The coexistence of blue and yellow bands across all concentrations further

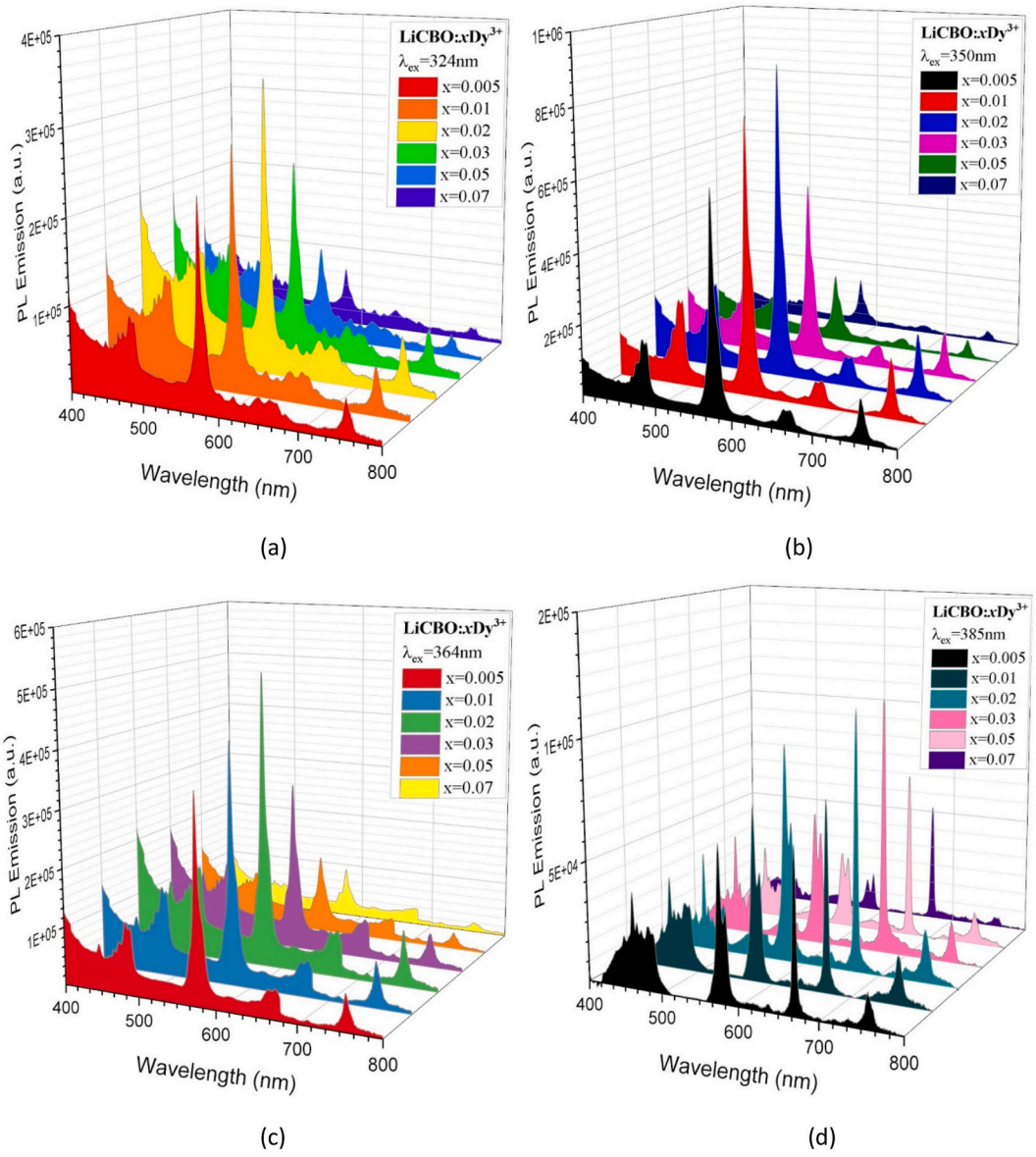

Fig. 4. Photoluminescence (PL) emission spectra of LiCBO:xDy^{3+} (x = 0.005–0.07) phosphors recorded under different excitation wavelengths: (a) 324 nm, (b) 350 nm, (c) 364 nm, and (d) 385 nm.

supports the potential of Dy^{3+}-activated LiCBO phosphors for white light generation. The strong emission under 385 nm excitation corresponds to the $^6H_{15/2} \rightarrow {}^6P_{7/2}$ absorption of Dy^{3+}, while the decrease at higher concentrations arises from Dy–Dy interactions leading to concentration quenching. The stable coexistence of blue (~480 nm) and yellow (~570 nm) bands suggests that the chromaticity coordinates remain favorable for white light generation.

3.5. *Influence of alkali Co-doping (K$^+$ and Na$^+$) on the PL emission of LiCBO:Dy^{3+}*

The effect of alkali co-doping on the photoluminescence (PL) emission of LiCBO:Dy^{3+} was examined under near-UV excitation at 385 nm (Fig. 6a and b). In both K$^+$- and Na$^+$-co-doped samples, the emission spectra retain the characteristic Dy^{3+} transitions ($^4F_{9/2} \rightarrow {}^6H_{15/2}$ at ~461 nm and $^4F_{9/2} \rightarrow {}^6H_{13/2}$ at ~576 nm), confirming that the activator ions continue to occupy Ca^{2+} lattice sites without altering their local symmetry. The addition of alkali ions significantly modifies the emission intensity.

In the K$^+$-co-doped series, the PL intensity increases up to y = 0.033, after which concentration quenching dominates due to enhanced Dy–Dy interactions and multipolar energy transfer among adjacent ions. A similar trend is observed for Na$^+$ incorporation, although the enhancement is more pronounced, with y = 0.03 producing the maximum emission intensity. This difference is attributed to the smaller ionic radius of Na$^+$ compared to K$^+$, which allows better accommodation in the lattice and more effective charge compensation of Dy^{3+} → Ca^{2+} substitutional defects, thereby reducing non-radiative recombination centers. In contrast, the relatively larger K$^+$ ions introduce greater local lattice strain, which limits the enhancement at higher concentrations. At excessive alkali levels (y ≥ 0.05), both series exhibit reduced emission owing to the activation of non-radiative channels and the onset of concentration quenching.

Comparable alkali co-doping effects have been reported in several Dy^{3+}-activated hosts, further supporting our observations. For example, in CaB_4O_7:Dy^{3+}, Li$^+$/K$^+$ incorporation enhances PL up to an optimal level before quenching occurs, attributed to improved charge compensation and local field modification (Altowyan et al., 2025b). Likewise, Rathina Mala et al. (Rathina Mala et al., 2023) demonstrated that $LiSrVO_4$:Dy^{3+} phosphors exhibit a pronounced PL enhancement upon

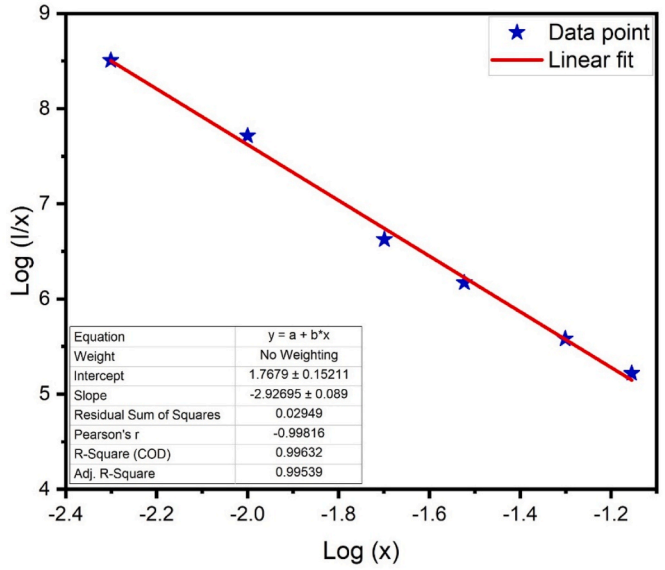

Fig. 5. Linear fitting of log(I/x) versus log(x) for LiCBO:xDy^{3+} phosphors, based on Dexter's theory of multipolar interactions.

$Li^+/Na^+/K^+$ co-doping, with Na^+ emerging as the most efficient charge compensator. This behavior is consistent with the present LiCBO:Dy^{3+} system, reinforcing that alkali-assisted charge compensation reduces non-radiative defects and enhances PL output.

These results confirm that alkali co-doping can effectively tune luminescence efficiency in LiCBO:Dy^{3+} phosphors, with Na^+ providing a superior improvement compared to K^+. The coexistence of stable blue and yellow bands across all compositions further underscores the potential of Dy^{3+}-activated LiCBO for white light generation.

3.6. Fluorescence lifetime analysis

Time-resolved luminescence measurements were carried out to elucidate the emission dynamics of Dy^{3+} in LiCBO with and without alkali co-doping. Fig. 7 displays the fluorescence decay curves, which were satisfactorily fitted using a multi-exponential model:

$$I(t) = \sum_{i=1}^{n} A_i \, exp\left(-\frac{t}{\tau_i}\right) \tag{4}$$

where A_i and τ_i are the amplitude and decay constant of the i^{th} component. The fitting quality, indicated by χ^2 values ranging from 1.40 to 1.85 (Table 3), confirms reliable deconvolution. The amplitude-weighted average lifetime was calculated according to:

$$\tau_{avg} = \frac{\sum A_i \tau_i^2}{\sum A_i \tau_i} \tag{5}$$

For singly Dy^{3+}-doped LiCBO, the average lifetimes increased systematically with activator content: 1725 μs (0.02Dy^{3+}) → 1876 μs (0.03Dy^{3+}) → 2048 μs (0.05Dy^{3+}). This monotonic increase suggests that higher Dy^{3+} incorporation enhances radiative probability by stabilizing excited states, while concentration quenching is not yet severe in the investigated range. The decay curves were dominated by long-lived components (τ_2,τ_3 ~ 0.6–3.0 ms), which accounted for ~70–80 % of the total contribution, whereas the short component (τ_1 ~ 15–17μs) is attributed to rapid quenching via defects or surface states.

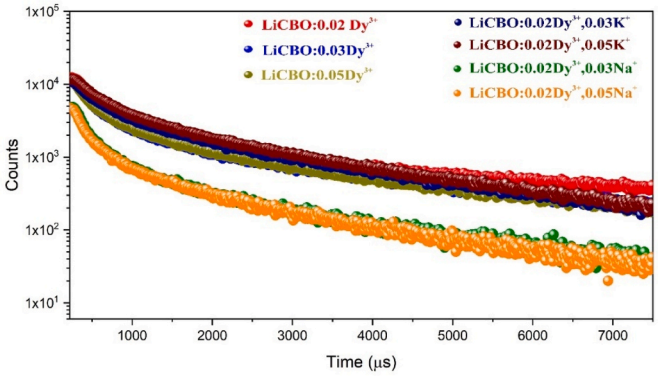

Fig. 7. Fluorescence decay curves of Dy^{3+}-doped and alkali co-doped LiCBO phosphors fitted with multi-exponential functions, showing the influence of Dy^{3+} concentration and Li^+/Na^+ co-doping on emission lifetimes.

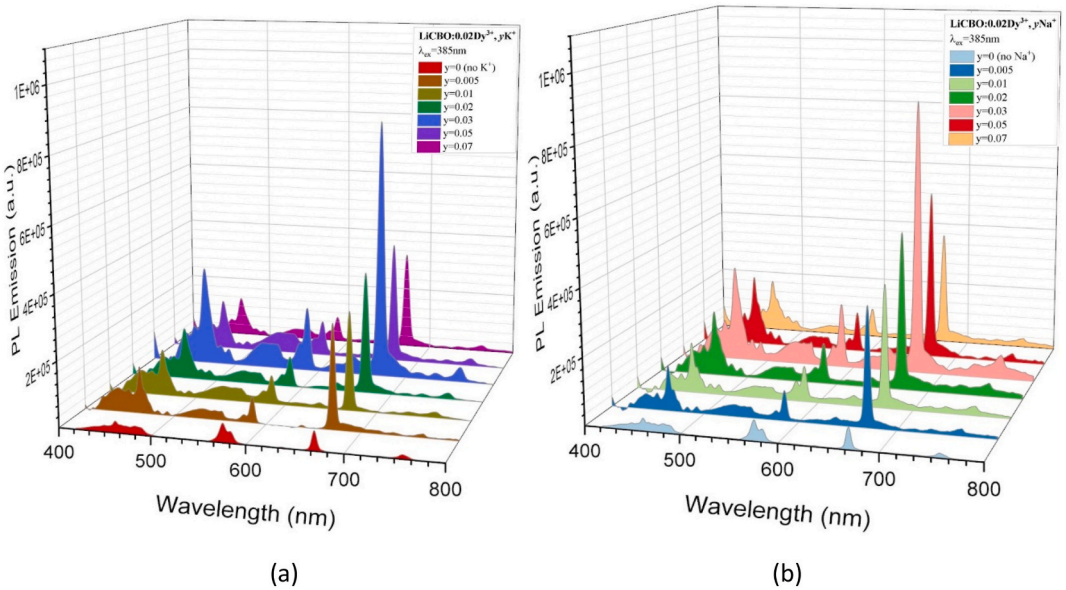

Fig. 6. (a) PL emission spectra of LiCBO:0.02Dy^{3+},yK^+ (y = 0–0.07) and (b) LiCBO:0.02Dy^{3+},yNa^+ (y = 0–0.07) phosphors excited at 385 nm, showing the characteristic Dy^{3+} blue ($^4F_{9/2} \rightarrow {}^6H_{15/2}$, ~461 nm) and yellow ($^4F_{9/2} \rightarrow {}^6H_{13/2}$, ~576 nm) transitions, with intensity variations governed by alkali co-doping and concentration quenching.

Table 3
Decay parameters and average lifetimes of Dy^{3+}-doped and alkali co-doped LiCBO phosphors obtained from multi-exponential fitting.

		Time(μs)	Rel.%	τ_{avg}(μs)	χ^2
LiCBO:0.02Dy^{3+}	τ_1	15.84	23.24	1724.558	1.8557
	τ_2	639.16	35.95		
	τ_3	2538.02	40.81		
LiCBO:0.03Dy^{3+}	τ_1	16.22	20.98	1875.944	1.5058
	τ_2	655.39	29.06		
	τ_3	2663.95	49.96		
LiCBO: 0.05Dy^{3+}	τ_1	16.99	20.80	2048.175	1.4793
	τ_2	721.74	30.76		
	τ_3	2977.77	48.44		
LiCBO:0.02Dy^{3+},0.03K^{+}	τ_1	25.49	26.12	1442.738	1.4079
	τ_2	1492.84	73.88		
LiCBO:0.02Dy^{3+},0.05K^{+}	τ_1	28.33	27.61	1490.239	1.5992
	τ_2	1545.97	72.39		
LiCBO:0.02Dy^{3+},0.03Na^{+}	τ_1	15.03	35.99	1110.971	1.5838
	τ_2	1172.58	64.01		
LiCBO:0.02Dy^{3+},0.05Na^{+}	τ_1	15.11	35.85	1111.921	1.6179
	τ_2	1173.23	64.15		

The effect of alkali co-doping was more complex. Li^{+} incorporation (0.03 and 0.05 wt%) reduced the average lifetimes to ~1443 and ~1490 μs, respectively, relative to the pristine 0.02 wt% Dy^{3+} sample. This reduction indicates that Li^{+} addition introduces additional non-radiative centers or enhances multipolar energy transfer between Dy^{3+} ions. In contrast, Na^{+} co-doping resulted in significantly shorter lifetimes of ~1111 μs for both 0.03 and 0.05 wt% Na^{+}. The nearly identical values suggest saturation behavior, where further Na^{+} addition does not strongly modify the decay kinetics. The stronger quenching in Na^{+}-co-doped samples compared to Li^{+} may be due to local crystal field distortions and increased probability of Dy^{3+}–Dy^{3+} non-radiative interactions.

Overall, these results demonstrate that while pure Dy^{3+} doping enhances emission lifetimes up to 0.05 wt%, alkali co-doping—particularly with Na^{+}—induces pronounced quenching effects that shorten the lifetime. The balance between charge compensation and defect generation thus critically governs the emission dynamics. From an application perspective, long-lived emissions observed in the singly Dy^{3+}-doped samples are advantageous for persistent luminescence and dosimetric applications, whereas alkali-assisted charge compensation strategies must be carefully optimized to avoid excessive non-radiative decay.

3.7. Judd–Ofelt analysis

The radiative properties of Dy^{3+} in LiCBO phosphors were analyzed within the framework of the Judd–Ofelt (J–O) theory (Judd, 1962; Ofelt, 1962). The $^4F_{9/2} \rightarrow {}^6H_{15/2}$ transition at 461 nm, which is of magnetic dipole (MD) character, was used as an internal reference with a standard spontaneous emission probability of $A_{MD} = 12.7\ s^{-1}$ (Carnall et al., 1968), while the $^4F_{9/2} \rightarrow {}^6H_{13/2}$ (576 nm), $^4F_{9/2} \rightarrow {}^6H_{11/2}$ (670 nm), and $^4F_{9/2} \rightarrow {}^6F_{11/2}/{}^6H_{9/2}$ (758 nm) bands were treated as electric dipole (ED) transitions. The experimental transition probabilities were obtained from the integrated emission intensities normalized to the MD line according to:

$$A_J^{exp} = A_{MD}\frac{\int I_J(\lambda)d\lambda}{I_{MD}(\lambda)d\lambda}\left(\frac{\lambda_{MD}}{\lambda_J}\right)^3 \quad (4)$$

and the theoretical ED probabilities were calculated as

$$A_J^{ED} = \frac{64\pi^4 e^2}{3h(2J+1)\lambda_J^3}\frac{n(n^2+2)^2}{9}\sum_{\lambda=2,4,6}\Omega_\lambda\langle U^{(\lambda)}\rangle^2 \quad (6)$$

where n = 1.65 is the refractive index and $\langle U^{(\lambda)}\rangle^2$ are the reduced matrix elements for Dy^{3+} taken from Carnall's free-ion data. From the fitted Ω_λ values, the radiative parameters were determined using

$$A_{tot} = \sum_J A_J, \tau_r = \frac{1}{A_{tot}}, \beta_J = \frac{A_J}{A_{tot}}, \eta_r = \frac{\tau_{exp}}{\tau_r} \quad (7)$$

The results show that for LiCBO:0.02Dy^{3+}, $\Omega_2 = 2.28 \times 10^{-20}\ cm^2$, $\Omega_4 = 4.35 \times 10^{-20}\ cm^2$, and $\Omega_6 = 1.92 \times 10^{-20}\ cm^2$, yielding branching ratios β (576 nm) = 0.58, β (670 nm) = 0.32, β(758 nm) = 0.10 and a radiative lifetime of 1820 μs in close agreement with the measured 1725 μs (η_r = 94.8 %), as summarized in Table 4. Upon K^{+} co-doping, Ω_2 increased to 2.61 while Ω_6 rose moderately to 2.15, leading to dominant yellow emission (β = 0.68 at 576 nm) with a noticeable increase in the far-red contribution (β = 0.13 at 758 nm). In contrast, Na^{+} co-doping reduced Ω_2 to 1.85 but significantly enhanced Ω_6 to 2.70, resulting in a redistribution of emission probability towards the red region, with β(670 nm) increasing from 0.32 to 0.68 and β(576 nm) decreasing from 0.58 to 0.23. The calculated radiative lifetime of 1160 μs again matched the experimental 1111 μs (η_r = 95.8 %). These results demonstrate that Na^{+} incorporation strengthens long-wavelength electric-dipole transitions through an increase in Ω_6, while K^{+} mainly preserves the hypersensitive yellow channel but also boosts the far-red band. The J–O analysis therefore explains the anomalous red enhancement observed in the PL spectra of Na- and K-co-doped samples, and the consistency between calculated and experimental lifetimes confirms that this redistribution is radiative in nature. The agreement with steady-state PL, where Na^{+} promotes strong red emission and K^{+} maintains bright yellow with moderate red contribution, further validates this interpretation. These findings are in line with previous reports: Guo et al. (2009) demonstrated that increasing Ω_6 values can induce red-shifts in the emission spectra of Dy^{3+}-doped chalcohalide glasses, and Zhang et al. (2024) reported that alkali modifiers in Dy^{3+}-doped borosilicate glasses systematically alter J–O parameters, with Na^{+} increasing Ω_6 and boosting long-wavelength emission. Overall, the present results establish that alkali co-doping, particularly with Na^{+}, is an effective route to tune the emission color of Dy^{3+} in LiCBO by modulating the balance between Ω_2 and Ω_6, providing a quantitative explanation consistent with PL spectra, decay dynamics, and structural findings.

3.8. High-temperature photoluminescence behavior

The temperature-dependent photoluminescence (PL) spectra of LiCOB:0.02Dy^{3+} and alkali ion co-doped derivatives (K^{+} and Na^{+}) are shown in Fig. 8. For the undoped LiCOB:0.02Dy^{3+} sample, the characteristic Dy^{3+} emission bands appear with dominant transitions at ~476 nm ($^4F_{9/2} \rightarrow {}^6H_{15/2}$) and 576 nm ($^4F_{9/2} \rightarrow {}^6H_{13/2}$), together with weaker red emissions near 646 nm and 752 nm. Interestingly, instead of conventional thermal quenching observed in most phosphors, the Dy^{3+}-only sample exhibits a continuous increase in PL intensity up to 550 K (Fig. 9a). This anomalous thermal enhancement is attributed to the thermally assisted release of carriers from shallow defect states, which recombine radiatively through Dy^{3+} levels and thus compensate non-radiative losses (Beck et al., 2017). As a consequence, Arrhenius fitting could not be applied to this system, and no activation energy (E_a) is reported.

In contrast, the K^{+}- and Na^{+}-co-doped samples show markedly different thermal responses. For the K^{+}-codoped composition, the PL intensity decreases up to ~420 K due to partial quenching, but a pronounced recovery occurs above 450 K, resulting in enhanced emission at higher temperatures (Fig. 9b). This recovery is explained by K^{+} induced charge-compensating defects and lattice vacancies, which act as carrier traps. At elevated temperatures, these traps release carriers that recombine through Dy^{3+} emission centers, thereby restoring luminescence. The Na^{+}-codoped sample exhibits a similar recovery profile (Fig. 9c), but with smoother and more stable thermal evolution. Above

Table 4
Judd–Ofelt parameters (Ω_2, Ω_4, Ω_6 in 10^{-20} cm^2), branching ratios (β), radiative lifetimes (τ_r, in μs), and radiative efficiencies (η_r in %) for Dy^{3+}-doped and alkali co-doped LiCBO phosphors.

Sample	Ω_2	Ω_4	Ω_6	β576(nm)	β670(nm)	β758(nm)	τ_r (μs)
LiCBO:0.02Dy^{3+}	2.28	4.35	1.92	0.58	0.32	0.10	1820
LiCBO:0.02Dy^{3+},0.03K^+	2.61	4.40	2.15	0.68	0.19	0.13	1505
LiCBO:0.02Dy^{3+},0.03Na^+	1.85	4.15	2.70	0.23	0.68	0.09	1160

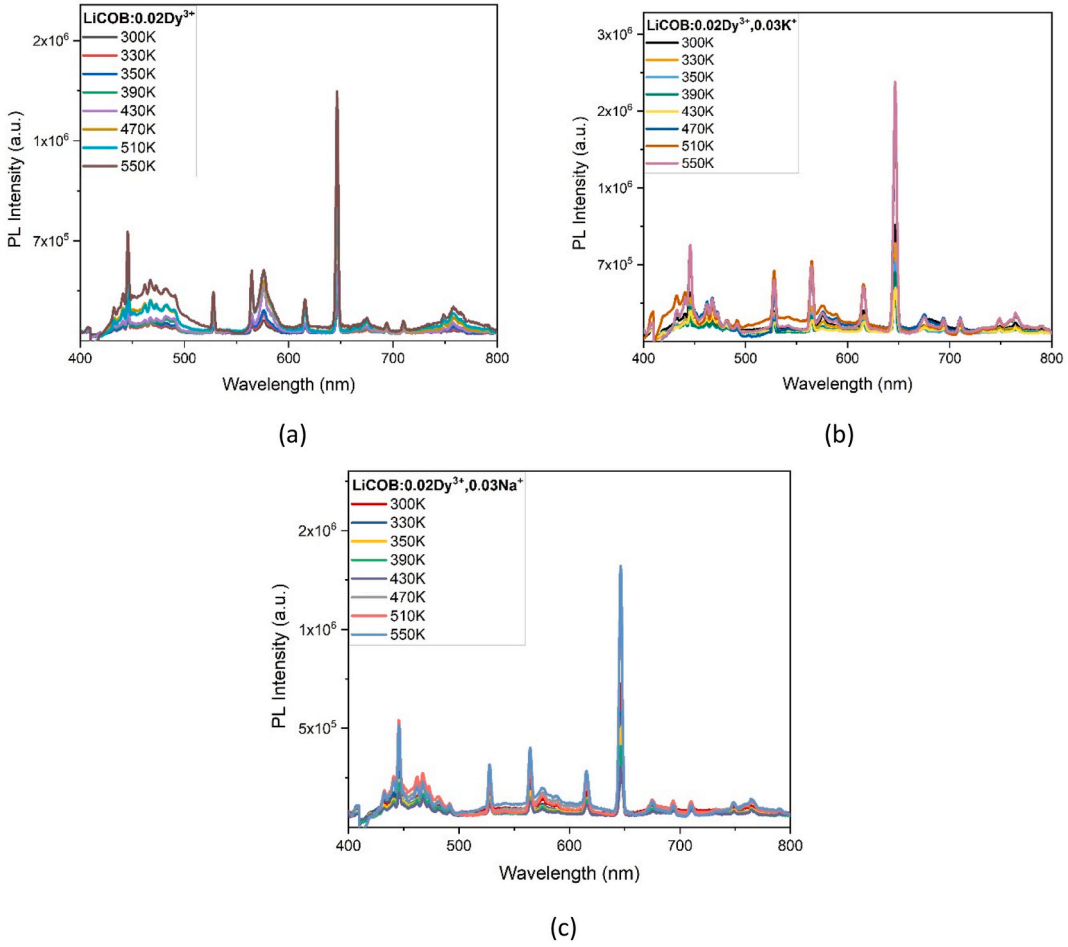

Fig. 8. Temperature-dependent PL spectra of (a) LiCOB:0.02Dy^{3+}, (b) LiCOB:0.02Dy^{3+},0.03K^+, and (c) LiCOB:0.02Dy^{3+},0.03Na^+ phosphors.

450 K, the PL intensity steadily increases, and by 550 K the emission nearly returns to its low-temperature level. This indicates that Na^+ generates a more favorable defect landscape, with shallow traps that enable efficient thermally stimulated emission.

The thermal quenching behaviour of the co-doped systems was further analyzed using the Arrhenius relation:

$$I(T) = \frac{I_0}{1 + Cexp(-E_a/k_B T)} \quad (8)$$

where I_0 is the initial PL intensity, C is a fitting constant, k_B is the Boltzmann constant, and E_a is the activation energy. Linearized plots of $\ln[(I_0/I) - 1]$ versus $1/k_BT$ (Fig. 10) yielded activation energies of $E_a \approx 0.219$ eV for the K^+-codoped sample and $E_a \approx 0.208$ eV for the Na^+-codoped sample, as summarized in Table 5. These relatively low barriers confirm that non-radiative thermal quenching is weak and that thermally released carriers dominate the high temperature PL process.

In summary, the Dy^{3+}-only system demonstrates anomalous thermal enhancement without a definable activation energy, whereas the alkali co-doped samples exhibit trap-assisted luminescence recovery with low activation energies (Table 5). These results demonstrate that alkali co-doping is an effective route to engineer defect structures and improve the high-temperature stability of Dy^{3+} emissions. Such behavior positions LiCOB:Dy^{3+}, particularly those modified with alkali ions, as strong candidates for thermally robust phosphor-converted white LEDs and optical thermometry applications.

3.9. CIE chromaticity analysis

The chromaticity coordinates of LiCBO:Dy^{3+} phosphors with varying Dy^{3+} concentrations and alkali ion co-doping were evaluated using the CIE 1931 diagram, as shown in Fig. 11. The calculated coordinates are listed in Table 6.

For the Dy^{3+}-only system (Fig. 11a), the emission coordinates gradually shift with increasing dopant concentration. At 0.02 Dy^{3+}, the phosphor exhibits coordinates (x = 0.3585, y = 0.3969), corresponding to near-white emission with a warm yellowish tint. At higher concentrations, the emission shifts toward lower x and y values, reflecting the concentration quenching and a reduced yellow contribution.

In the case of K^+ co-doping (Fig. 11b), the chromaticity points are

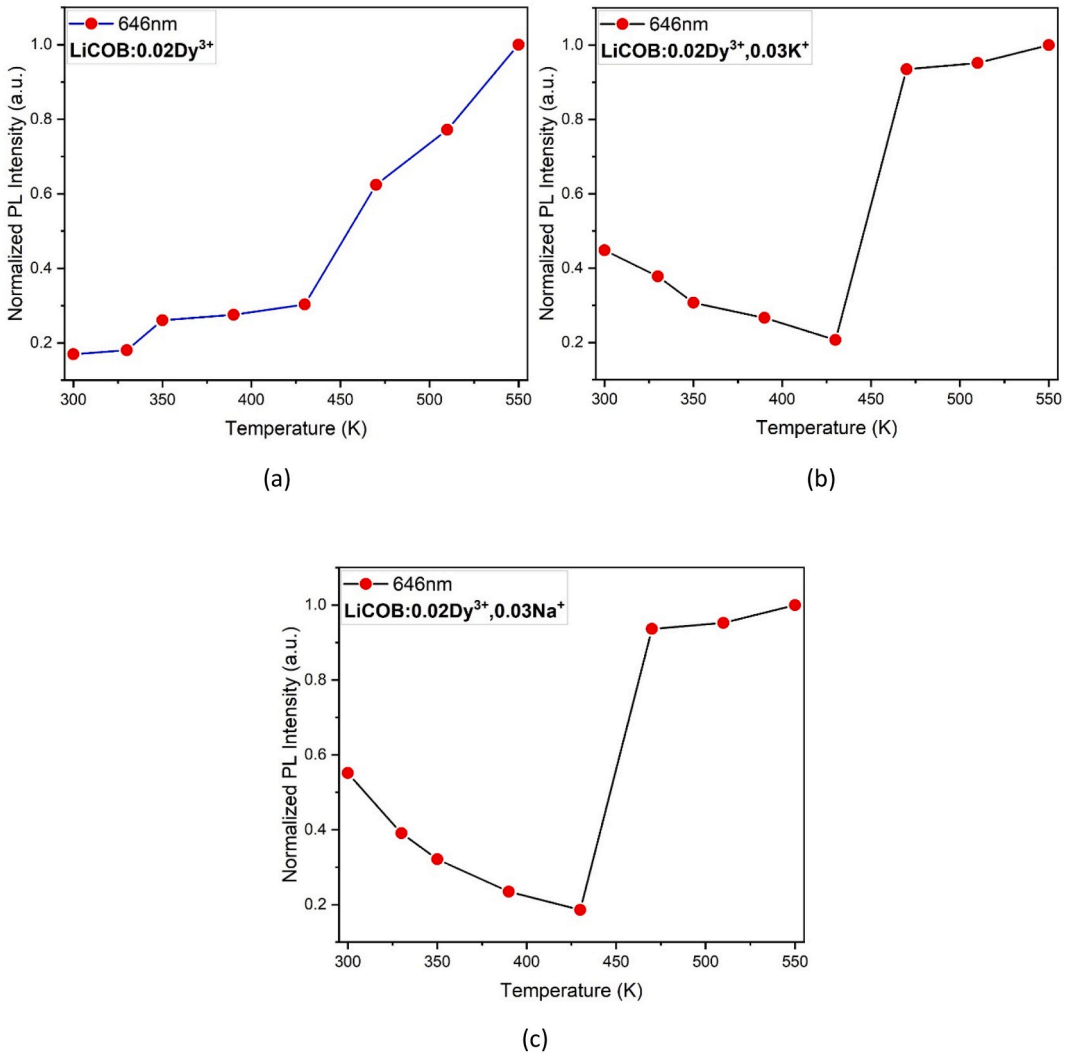

Fig. 9. Normalized PL intensity at 646 nm as a function of temperature for (a) LiCOB:0.02Dy^{3+}, showing anomalous thermal enhancement, (b) LiCOB:0.02Dy^{3+},0.03K^{+}, exhibiting trap-assisted recovery after partial quenching, and (c) LiCOB:0.02Dy^{3+},0.03Na^{+}, showing smoother recovery behavior.

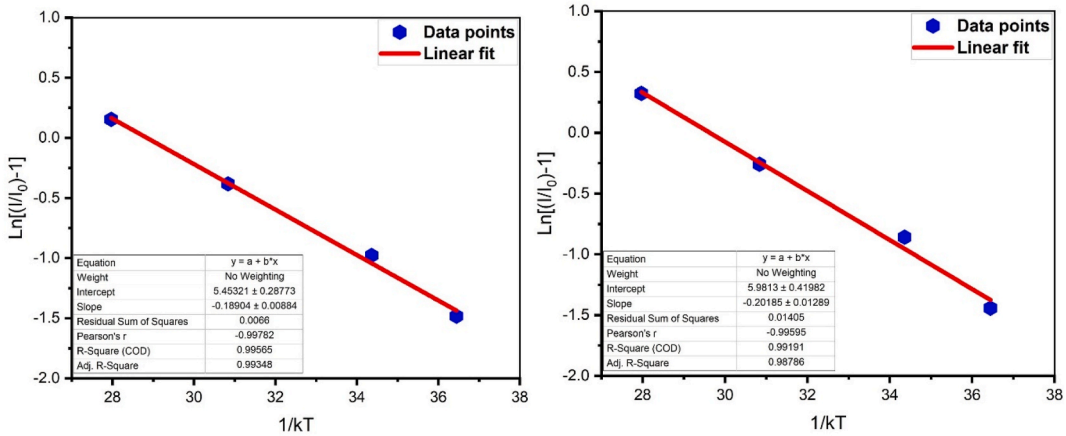

Fig. 10. Arrhenius plots of ln[(I_0/I) – 1] versus 1/k_BT for (a) LiCOB:0.02Dy^{3+},0.03K^{+} and (b) LiCOB:0.02Dy^{3+},0.03Na^{+} phosphors.

significantly displaced compared to the Dy^{3+}-only reference. The coordinates move toward lower x values with increasing K^{+} content, stabilizing in the bluish-white region. This shift confirms that K^{+} incorporation modifies the local crystal field and introduces charge-compensating defects that redistribute the Dy^{3+} emission probabilities. The broad range of accessible chromaticity coordinates under K^{+} modification indicates tunability from warm white to near-cool white emission.

Na^{+} co-doping (Fig. 11c) exhibits a similar evolution, but with coordinates shifted further towards the blue-green region compared to K^{+}.

Table 5
Activation energies (E_a) obtained from Arrhenius fitting of temperature-dependent PL intensity for LiCOB:0.02Dy^{3+},0.03K^+ and LiCOB:0.02Dy^{3+},0.03Na^+.

Sample	Activation energy, E_a (eV)
LiCOB:0.02Dy^{3+}	Not evaluated (anomalous thermal enhancement)
LiCOB:0.02Dy^{3+}, 0.03K^+	~0.219
LiCOB:0.02Dy^{3+}, 0.03Na^+	~0.208

For instance, at 0.02 Na^+, the CIE point lies at (x = 0.2872, y = 0.2948), closer to the ideal daylight white coordinates. With higher Na^+ concentrations, the points stabilize around (x ≈ 0.27, y ≈ 0.27), signifying improved color stability and enhanced long-wavelength contribution from Dy^{3+}.

In summary, the CIE analysis shows that Dy^{3+} concentration alone tunes the emission from cool to warm white, peaking at 0.02 Dy^{3+}. Alkali co-doping, on the other hand, drives the chromaticity back toward cooler tones, with K^+ producing more scattered shifts and Na^+ yielding a smoother, more stable evolution. Notably, the Na^+-codoped samples exhibit coordinates approaching the white-light region (close to the standard illuminant D65), underlining their suitability for phosphor-converted white LEDs. These results confirm that alkali modification provides a versatile means of tailoring the emission color of Dy^{3+}-doped LiCBO phosphors, supporting their potential in solid-state lighting applications.

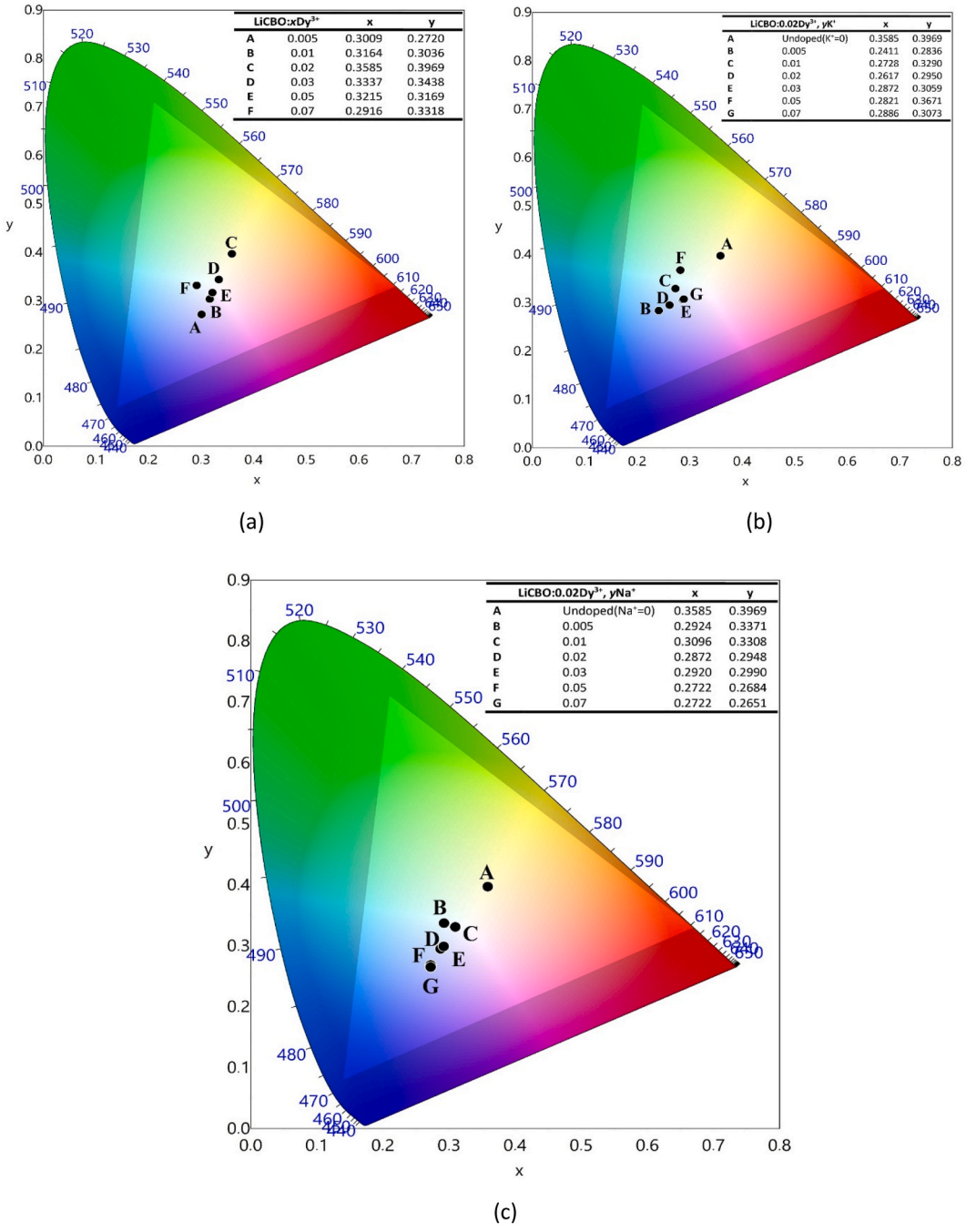

Fig. 11. CIE 1931 chromaticity coordinates for (a) LiCOB:xDy^{3+} (x = 0.005–0.07), (b) LiCOB:0.02Dy^{3+}, yK^+, and (c) LiCOB:0.02Dy^{3+}, yNa^+ phosphors; inset values show the calculated coordinates.

Table 6
CIE chromaticity coordinates (x,y) and CCT for LiCOB:xDy^{3+}, LiCBO:0.02Dy^{3+}, yK^{+} and LiCBO:0.02Dy^{3+}, yNa $^{+}$ phosphors.

Dy^{3+} content (wt.%)	x	y	CCT
x = 0.005	0.3009	0.2720	8461
x = 0.01	0.3164	0.3036	6483
x = 0.02	0.3585	0.3969	4716
x = 0.03	0.3337	0.3438	5446
x = 0.05	0.3215	0.3169	6087
x = 0.07	0.2916	0.3318	7688
K^{+} content (wt.%)	**x**	**y**	**CCT**
y = 0.005	0.2411	0.2836	15279
y = 0.01	0.2728	0.3290	8973
y = 0.02	0.2617	0.2950	11498
y = 0.03	0.2872	0.3059	8579
y = 0.05	0.2821	0.3671	7676
y = 0.07	0.2886	0.3073	8428
Na $^{+}$ content (wt.%)	**x**	**y**	**CCT**
y = 0.005	0.2924	0.3371	7555
y = 0.01	0.3096	0.3308	6656
y = 0.02	0.2872	0.2948	8952
y = 0.03	0.2920	0.2990	8388
y = 0.05	0.2722	0.2684	12488
y = 0.07	0.2722	0.2651	12878

4. Conclusion

In this study, Dy^{3+}-doped $LiCaBO_3$ phosphors were successfully synthesized and comprehensively characterized, with particular attention to the effects of alkali ion (Na^+, K^+) co-doping. Structural analysis confirmed that Dy^{3+} ions preferentially substitute Ca^{2+} sites, and that alkali co-doping effectively compensates charge imbalance while reducing lattice strain. Vibrational studies corroborated the preservation of the borate framework, with Na $^{+}$ proving to be the most efficient stabilizer. Photoluminescence investigations demonstrated intense blue and yellow Dy^{3+} emissions, enabling quasi-white light generation with optimal performance at 2 wt% doping. Concentration quenching was shown to proceed via dipole–quadrupole interactions, while Judd–Ofelt analysis revealed that alkali modifiers tune the radiative properties by selectively enhancing Ω_2 or Ω_6 parameters, thereby redistributing emission probabilities. Temperature-dependent PL measurements highlighted the unusual thermal enhancement in undoped samples and trap-assisted recovery in co-doped systems, underscoring the excellent thermal stability of the materials. Taken together, these results demonstrate that alkali co-doping not only improves the luminescence efficiency of $LiCaBO_3$:Dy^{3+} but also enables controlled spectral tuning with stable chromaticity. In addition to their relevance for solid-state lighting, the observed high-temperature luminescence response suggests promising potential for radiation detector applications.

CRediT authorship contribution statement

M.B. Coban: Investigation, Methodology, Software. **Jabir Hakami:** Conceptualization, Data curation, Investigation. **H. Aydin:** Investigation, Methodology, Software. **U.H. Kaynar:** Investigation, Methodology, Software, Visualization. **E. Aymila Çin:** Formal analysis. **T. Karaman:** Formal analysis. **M. Sharahili:** Investigation, Methodology. **O. Madkhali:** Investigation, Methodology. **D. Somaily:** Investigation, Methodology. **Rachid Karmouch:** Conceptualization, Investigation. **N. Can:** Funding acquisition, Investigation, Methodology, Supervision, Writing – original draft, Writing – review & editing.

Declaration of competing interest

The authors declare that they have no known competing financial interests or personal relationships that could have appeared to influence the work reported in this paper.

Acknowledgements

The authors gratefully acknowledge the funding of the Deanship of Graduate Studies and Scientific Research, Jazan University, Saudi Arabia, through Project number: (JU-20250218-DGSSR-RP-2025).

Data availability

Data will be made available on request.

References

Adeleye, S.O., Adeleke, A.A., Nzerem, P., Olosho, A.I., Anosike-Francis, E.N., Ogedengbe, T.S., Ikubanni, P.P., Saleh, R.A., Okolie, J.A., 2024. A review of the physical, optical and photoluminescence properties of rare Earth ions doped glasses. Trends Sci. 21, 8759. https://doi.org/10.48048/tis.2024.8759.

Aljewaw, O.B., Karim, M.K.A., Effendy, N., Kamari, H.M., Zaid, M.H.M., Noor, N.M., Salim, A.A., Isa, N.M., Kadir, A.B.A., Chew, M.T., Abokridiga, A.I., 2023. Physical, optical and thermoluminescence properties of lithium aluminum borate glass co-doped with Dy_2O_3. Radiat. Phys. Chem. 209, 111004. https://doi.org/10.1016/j.radphyschem.2023.111004.

Altowyan, A.S., Aydin, H., Kaynar, U.H., Coban, M.B., Hakami, J., Townsend, P.D., Can, N., 2025a. Structural, thermal, and optical properties of Dy^{3+}/K^{+} Co-Doped $SmCa_4O(BO_3)_3$ phosphors synthesized by sol-gel method. Adv. Powder Technol. 36, 104905. https://doi.org/10.1016/j.apt.2025.104905.

Altowyan, A.S., Kaynar, U.H., Aydin, H., Hakami, J., Coban, M.B., Cikrikci, K., Ayvacikli, M., Can, N., 2025b. Synthesis, structural characterization, and photoluminescence properties of Dy3+-Doped CaB4O7 phosphors: influence of Li+ and K+ Co-doping. Mater. Sci. Semicond. Process. 195, 109593. https://doi.org/10.1016/j.mssp.2025.109593.

Altowyan, A.S., Kaynar, U.H., Gök, C., Aydin, H., Hakami, J., Coban, M.B., Canimoglu, A., Can, N., 2025c. Photoluminescence characteristics and Judd–Ofelt analysis of $YBa_3(BO_3)_3$:Tb^{3+} phosphors co-doped with Li^{+}, Na^{+}, and K^{+}. J. Lumin. 286, 121380. https://doi.org/10.1016/j.jlumin.2025.121380.

Ayvacikli, M., Kaynar, Ü.H., Karabulut, Y., Garcia Guinea, J., Bulcar, K., Can, N., 2020a. Cathodoluminescence properties of La_2MoO_6:Ln^{3+} (Ln: eu, Dy, and sm) phosphors. Appl. Radiat. Isot. 166, 109434. https://doi.org/10.1016/j.apradiso.2020.109434.

Ayvacikli, M., Kaynar, Ü.H., Karabulut, Y., Guinea, J.G., Dogan, T., Can, N., 2020b. Cathodoluminescence and photoluminescence properties of Dy doped $La_2CaB_{10}O_{19}$ phosphor. Opt. Mater. 110, 110531. https://doi.org/10.1016/j.optmat.2020.110531.

Bajaj, N.S., Omanwar, S.K., 2012. Combustion synthesis and luminescence characteristic of rare earth activated $LiCaBO_3$. J. Rare Earths 30, 1005–1008. https://doi.org/10.1016/S1002-0721(12)60169-0.

Beck, A.R., Das, S., Manam, J., 2017. Temperature dependent photoluminescence of Dy^{3+} doped $LiCaBO_3$ phosphor. J. Mater. Sci. Mater. Electron. 28, 17168–17176. https://doi.org/10.1007/s10854-017-7645-4.

Blasse, G., Grabmaier, B.C., 1994. Luminescent Materials. Springer Berlin Heidelberg, Berlin, Heidelberg. https://doi.org/10.1007/978-3-642-79017-1.

Boronat, C., Correcher, V., Bravo-Yagüe, J.C., Sarasola-Martin, I., Garcia-Guinea, J., Benavente, J.F., 2023. Comparing the effect of electron beam, beta and ultraviolet C exposure on the luminescence emission of commercial dosimeters. Spectrochim. Acta Mol. Biomol. Spectrosc. 295, 122571. https://doi.org/10.1016/j.saa.2023.122571.

Carnall, W.T., Fields, P.R., Rajnak, K., 1968. Electronic energy levels of the Trivalent lanthanide Aquo ions. IV. Eu^{3+}. J. Chem. Phys. 49, 4450–4455. https://doi.org/10.1063/1.1669896.

Chen, C., Wu, Y., Jiang, A., Wu, B., You, G., Li, R., Lin, S., 1989. New nonlinear-optical crystal: LiB_3O_5. J. Opt. Soc. Am. B 6, 616. https://doi.org/10.1364/JOSAB.6.000616.

Ćirić, A., Stojadinović, S., Sekulić, M., Dramićanin, M.D., 2019. JOES: an application software for Judd-Ofelt analysis from Eu^{3+} emission spectra. J. Lumin. 205, 351–356. https://doi.org/10.1016/j.jlumin.2018.09.048.

Dexter, D.L., 1953. A theory of sensitized luminescence in solids. J. Chem. Phys. 21, 836–850. https://doi.org/10.1063/1.1699044.

Garcia-Guinea, J., Garrido, F., Lopez-Arce, P., Correcher, V., de la Figuera, J., 2017. Spectral green cathodoluminescence emission from surfaces of insulators with metal-hydroxyl bonds. J. Lumin. 190, 128–135. https://doi.org/10.1016/j.jlumin.2017.05.039.

Guo, H., Liu, L., Wang, Y., Hou, C., Li, W., Lu, M., Zou, K., Peng, B., 2009. Host dependence of spectroscopic properties of Dy^{3+}-doped and Dy^{3+}, Tm^{3+}-codoped Ge–Ga–S–CdI$_2$ chalcohalide glasses. Opt. Express 17 (17), 15350–15358. https://doi.org/10.1364/OE.17.015350.

Jiang, L.H., Zhang, Y.L., Li, C.Y., Pang, R., Hao, J.Q., Su, Q., 2008. Thermoluminescence characteristics of rare-earth-doped $LiCaBO_3$ phosphor. J. Lumin. 128, 1904–1908. https://doi.org/10.1016/j.jlumin.2008.05.017.

Judd, B.R., 1962. Optical absorption intensities of rare-earth ions. Phys. Rev. 127, 750–761. https://doi.org/10.1103/PhysRev.127.750.

Khan, Z.S., Ingale, N.B., Omanwar, S.K., 2016. Synthesis and thermoluminescence properties of rare earth-doped $NaMgBO_3$ phosphor. Environ. Sci. Pollut. Res. 23, 9295–9302. https://doi.org/10.1007/s11356-015-4993-6.

Kumar, Amit Anu, Lohan, R., Rani, U., Malik, I., Deopa, N., Rao, A.S., Kumar, Anand, 2025. Dysprosium ion concentration variations and their comprehensive influence on the physical, structural and optical properties of multi-component borate glasses for luminescence tailoring. Ceram. Int. 51, 16509–16523. https://doi.org/10.1016/j.ceramint.2024.10.123.

Li, P., Wang, Z., Yang, Z., Guo, Q., Li, X., 2010. Luminescent characteristics of $LiCaBO_3$:M (M=Eu^{3+}, Sm3+, Tb^{3+}, Ce^{3+}, Dy^{3+}) phosphor for white LED. J. Lumin. 130, 222–225. https://doi.org/10.1016/j.jlumin.2009.08.010.

Li, P., Yang, Z., Wang, Z., Guo, Q., 2009. Luminescent characteristics of $LiCaBO_3$:Eu^{3+} phosphor for white light emitting diode. J. Rare Earths 27, 390–393. https://doi.org/10.1016/S1002-0721(08)60257-4.

Liang, P., Liu, J.W., Liu, Z.H., 2016. Controllable hydrothermal synthesis of Eu^{3+}/Tb^{3+}/Dy^{3+} activated Zn $_8[(BO_3)_3O_2(OH)_3$] micro/nanostructured phosphors: energy transfer and tunable emissions. RSC Adv. 6, 89113–89123. https://doi.org/10.1039/C6RA19101K.

Luewarasirikul, N., Sarachai, S., Intachai, N., Kothan, S., Djamal, M., Kaewkhao, J., 2026. Effect of Dy^{3+} concentration on the luminescence properties of Dy^{3+}/Gd^{3+} co-doped in barium sodium borate glass scintillators. Radiat. Phys. Chem. 239, 113282. https://doi.org/10.1016/j.radphyschem.2025.113282.

Luo, M., Chen, B., Li, X., Zhang, J., Xu, S., Zhang, X., Cao, Y., Sun, J., Zhang, Yanqiu, Wang, X., Zhang, Yuhang, Gao, D., Wang, L., 2020. Fluorescence decay route of optical transition calculation for trivalent rare earth ions and its application for Er 3 + -doped NaYF 4 phosphor. Phys. Chem. Chem. Phys. 22, 25177–25183. https://doi.org/10.1039/D0CP04379F.

Luo, W., Liao, J., Li, R., Chen, X., 2010. Determination of Judd–Ofelt intensity parameters from the excitation spectra for rare-earth doped luminescent materials. Phys. Chem. Chem. Phys. 12, 3276. https://doi.org/10.1039/b921581f.

Mastanappa, A., Biradar, S., Devidas, G.B., Rajaramakrishna, R., Sayyed, M.I., Chandrashekara, M.N., 2024. Effect of Li_2O on physical, structural, thermal, optical, and electrical properties of mixed alkali borate glasses containing silver nanoparticles. Opt. Mater. 157, 116224. https://doi.org/10.1016/j.optmat.2024.116224.

Nasreen, S., Mahamuda, S., Dedeepya, G., Swapna, K., Venkateswarlu, M., Rao, A.S., 2025. Effect of barium fluoride on efficiency of Dy3+ ions doped titanium borate glasses. Mater. Lett. 388, 138291. https://doi.org/10.1016/j.matlet.2025.138291.

Ofelt, G.S., 1962. Intensities of Crystal spectra of rare-earth ions. J. Chem. Phys. 37, 511–520. https://doi.org/10.1063/1.1701366.

Oza, A.H., Dhoble, N.S., Lochab, S.P., Dhoble, S.J., 2015. Luminescence study of Dy or Ce activated LiCaBO 3 phosphor for γ-ray and C 5+ ion beam irradiation. Luminescence 30, 967–977. https://doi.org/10.1002/bio.2846.

Padlyak, B., Drzewiecki, A., 2013. Spectroscopy of the CaB4O7 and LiCaBO3 glasses, doped with terbium and dysprosium. J. Non-Cryst. Solids 367, 58–69. https://doi.org/10.1016/j.jnoncrysol.2013.02.018.

Rathina Mala, V., Balakrishnan, P., Masilla Moses Kennedy, S., 2023. Effect of co-doping alkali metal ions Li^+/Na^+/K^+ on the photoluminescence enhancement properties of the near white light emitting $LiSrVO_4$:Dy^{3+} phosphor along with the optical transition probabilities by Judd-Ofelt analysis for WLEDs application. Solid State Sci. 138, 107131. https://doi.org/10.1016/j.solidstatesciences.2023.107131.

Roman-Lopez, J., Correcher, V., Garcia-Guinea, J., Rivera, T., Lozano, I.B., 2012. Cathodoluminescence and green-thermoluminescence response of $CaSO_4$:Dy,P films. J. Lumin. 135, 89–92. https://doi.org/10.1016/j.jlumin.2012.10.020.

Sharma, M., Sharma, H., Charak, I., Swart, H.C., Kumar, V., 2024. Optimization and luminescence studies of Sm^{3+} doped $LiCaBO_3$ phosphors for high-performance white light-emitting diodes. Chem. Phys. Impact 9, 100696. https://doi.org/10.1016/j.chphi.2024.100696.

Wang, Y., Liu, X., Jing, L., Niu, P., 2016. Tunable white light and energy transfer of Dy^{3+} and Eu^{3+} doped $Y_2Mo_4O_{15}$ phosphors. Ceram. Int. 42, 13004–13010. https://doi.org/10.1016/j.ceramint.2016.05.075.

Xue, S.-D., Liu, M.-H., Zhang, P., Wong, W.-H., Zhang, D.-L., 2020. Validity of Judd-Ofelt spectroscopy based on diffuse reflectance spectrum and fluorescence lifetime of phosphor. J. Lumin. 224, 117304. https://doi.org/10.1016/j.jlumin.2020.117304.

Yen, W., Shionoya, S., Yamamoto, H., 2007. In: Phosphor Handbook, second ed. CRC Press.

Zhang, X., Lin, H., Li, S., He, J., Li, C., Liu, L., Yang, W., Zeng, F., 2024. Judd-ofelt analysis and luminescent properties of the Dy^{3+}-doped borosilicate glass. Opt. Mater. 151, 115366. https://doi.org/10.1016/j.optmat.2024.115366.